The Astrophysical Journal Supplement Series, 247:67 (11pp), 2020 April https://doi.org/10.3847/1538-4365/ab77b1

Imaging and Modeling Data from the Hydrogen Epoch of Reionization Array

C. L. Carilli[1,2], N. Thyagarajan[1], J. Kent[2], B. Nikolic[2], K. Gale-Sides[2], N. S. Kern[3], G. Bernardi[4,5,6], A. Mesinger[7], S. Matika[5], Zara Abdurashidova[3], James E. Aguirre[8], Paul Alexander[2], Zaki S. Ali[3], Yanga Balfour[6], Adam P. Beardsley[9], Tashalee S. Billings[8], Judd D. Bowman[9], Richard F. Bradley[1], Phil Bull[10], Jacob Burba[11], Carina Cheng[3], David R. DeBoer[3], Matt Dexter[3], Eloy de Lera Acedo[2], Joshua S. Dillon[3], Aaron Ewall-Wice[12], Nicolas Fagnoni[1], Randall Fritz[6], Steve R. Furlanetto[13], Kingsley Gale-Sides[2], Brian Glendenning[1], Deepthi Gorthi[3], Bradley Greig[14], Jasper Grobbelaar[6], Ziyaad Halday[6], Bryna J. Hazelton[15,16], Jacqueline N. Hewitt[12], Jack Hickish[3], Daniel C. Jacobs[9], Alec Josaitis[2], Austin Julius[6], Joshua Kerrigan[11], Honggeun Kim[12], Piyanat Kittiwisit[9], Saul A. Kohn[8], Matthew Kolopanis[9], Adam Lanman[11], Paul La Plante[8], Telalo Lekalake[6], Adrian Liu[17], David MacMahon[3], Lourence Malan[6], Cresshim Malgas[6], Matthys Maree[6], Zachary E. Martinot[8], Eunice Matsetela[6], Mathakane Molewa[6], Miguel F. Morales[15], Tshegofalang Mosiane[6], Abraham R. Neben[12], Juan Mena Parra[12], Aaron R. Parsons[3], Nipanjana Patra[3], Samantha Pieterse[6], Jonathan C. Pober[11], Nima Razavi-Ghods[2], James Robnett[1], Kathryn Rosie[6], Peter Sims[11], Angelo Syce[6], Peter K. G. Williams[18], and Haoxuan Zheng[12]

[1] National Radio Astronomy Observatory, P.O. Box 0, Socorro, NM 87801, USA; ccarilli@nrao.edu
[2] Astrophysics Group, Cavendish Laboratory, JJ Thomson Avenue, Cambridge CB3 0HE, UK
[3] Department of Astronomy, University of California, Berkeley, CA, USA
[4] INAF-Istituto di Radioastronomia, via Gobetti 101, I-40129, Bologna, Italy
[5] Department of Physics and Electronics, Rhodes University, P.O. Box 94, Grahamstown, 6140, South Africa
[6] The South African Radio Astronomy Observatory (SARAO), 2 Fir Street, Black River Park, Observatory (North Gate entrance), 7925, South Africa
[7] Scuola Normale Superiore, I-56126 Pisa, PI, Italy
[8] Department of Physics and Astronomy, University of Pennsylvania, Philadelphia, PA, USA
[9] School of Earth and Space Exploration, Arizona State University, Tempe, AZ, USA
[10] Queen Mary University of London, London, UK
[11] Department of Physics, Brown University, Providence, RI, USA
[12] Department of Physics, Massachusetts Institute of Technology, Cambridge, MA, USA
[13] Department of Physics and Astronomy, University of California, Los Angeles, CA, USA
[14] School of Physics, University of Melbourne, Parkville, VIC 3010, Australia
[15] Department of Physics, University of Washington, Seattle, WA, USA
[16] eScience Institute, University of Washington, Seattle, WA, USA
[17] Department of Physics and McGill Space Institute, McGill University, 3600 University Street, Montreal, QC H3A 2T8, Canada
[18] Harvard-Smithsonian Center for Astrophysics, Cambridge, MA, USA

Received 2019 August 29; revised 2020 February 14; accepted 2020 February 17; published 2020 April 7

Abstract

We analyze data from the Hydrogen Epoch of Reionization Array (HERA). This is the third in a series of papers on the closure phase delay spectrum technique designed to detect the H I 21 cm emission from cosmic reionization. We present the details of the data and models employed in the power spectral analysis and discuss limitations to the process. We compare images and visibility spectra made with HERA data to parallel quantities generated from sky models based on the Galactic and Extra-Galactic All-Sky MWA (GLEAM) survey, incorporating the HERA telescope model. We find reasonable agreement between images made from HERA data with those generated from the models, down to the confusion level. For the visibility spectra, there is broad agreement between model and data across the full band of ~80 MHz. However, models with only GLEAM sources do not reproduce a roughly sinusoidal spectral structure at the tens of percent level seen in the observed visibility spectra on scales of ~10 MHz on 29 m baselines. We find that this structure is likely due to diffuse Galactic emission, predominantly the Galactic plane, filling the far sidelobes of the antenna primary beam. We show that our current knowledge of the frequency dependence of the diffuse sky radio emission, and the primary beam at large zenith angles, is inadequate to provide an accurate reproduction of the diffuse structure in the models. We discuss some implications arising due to this missing structure in the models, in terms of calibration, and in the search for the H I 21 cm signal, as well as possible mitigation techniques.

Unified Astronomy Thesaurus concepts: Cosmology (343); Cosmological evolution (336); Radio interferometry (1346); Reionization (1383)

1. Introduction

Cosmic reionization corresponds to the epoch when the ultraviolet (UV) radiation from the first luminous sources (stars and black holes) reionizes the neutral hydrogen that pervaded the universe after cosmic recombination. Measurements of quasar absorption lines, Lyα galaxy demographics, and the cosmic microwave background have constrained the redshift at which the ionization fraction reaches 50% in the intergalactic medium (IGM) to be $z = 8.1 \pm 1$, with a duration (from 25% to 75% ionized) of $\Delta z \sim \pm 1$ (Greig & Mesinger 2017). While the basic epoch and duration of reionization are reasonably well constrained, many important questions remain about the process of reionization (e.g., inside-out or outside-in?) and the sources of reionization (e.g., small galaxies, big galaxies, low to intermediate mass black holes?).

It is widely recognized that the 21 cm line of neutral hydrogen is a potentially powerful probe of the physics of cosmic reionization (Fan et al. 2006; Morales & Wythie 2010;

Loeb & Furlanetto 2013). Imaging at low radio frequencies (100–200 MHz) has the potential to determine the large-scale structure of the universe, as dictated by the combined processes of dark matter evolution and reionization. Numerous interferometric experiments are currently operating with the goal of making the first statistical (i.e., power spectral) detection of the H I 21 cm signal from large-scale structure in the universe during cosmic reionization (Beardsley et al. 2016; DeBoer et al. 2017; Patil et al. 2017; Barry et al. 2019; Kolopanis et al. 2019; Li et al. 2019; Trott et al. 2020).

A major hurdle to making the first H I 21 cm detection remains: removal of the strong foreground radio continuum emission, corresponding to radio synchrotron emission from the Milky Way and from distant radio galaxies. The foregrounds have a mean surface brightness four to five orders of magnitude larger than the H I 21 cm signal, even in the quietest parts of the sky. Different experiments are employing varied techniques to obtain this first detection. The originally proposed technique, outlined in e.g., Tegmark (1997), Morales (2005), and Harker et al. (2009, 2010; see the reviews in Furlanetto et al. 2006; Morales & Wythie 2010; Zaroubi 2013), employs calculating the three-dimensional power spectrum from image cubes, where the three space dimensions in the image cube (R.A., decl., and frequency, the latter of which corresponds to distance via the redshift of the H I 21 cm line) transform to the conjugate wavenumber (k) in power spectrum space. The image cubes are generated from the interferometric data via the standard Fourier transform relationship between visibilities and sky-plane surface brightness. The radio continuum emission is subtracted via multiple processes, including identification of point sources in the image domain, then "peeling" these sources in the *uv* plane (Noordam 2004), as well as subtracting smooth spectrum models fit to the image cubes, or visibilities, themselves (Zaldarriaga et al. 2004; Chapman et al. 2013). Variants of these techniques have been employed in the recent analysis of Low Frequency Array (LOFAR) data by (Patil et al. 2017), who calculate both the cylindrical (i.e., line of sight; see below) and the spherical (i.e., three-dimensional) power spectrum. At the other extreme is the "delay spectrum" approach, employing the relationship between the frequency and cosmic distance (i.e., redshift) to obtain a power spectrum of the H I 21 cm signal from the Fourier transform of interferometric visibility spectra along the frequency axis. In this case, since the baseline is fixed, there will be spatial "mode-mixing" as a function of frequency, but this effect is minor on short spacings and moderate frequency ranges. In this "delay space" (where delay is the Fourier conjugate of frequency), the smooth spectrum foreground continuum emission is naturally limited to small delays ($\sim k_{\parallel}$-modes), although the real and imaginary parts of a given visibility will have a frequency structure due to continuum sources not at the phase tracking center (Datta et al. 2010; Parsons et al. 2014; Morales et al. 2019).

In a series of papers, we are presenting a new approach to the H I 21 cm detection, namely, using the closure phase spectra to obtain a power spectral detection of the H I 21 cm emission from reionization. Our technique parallels the delay spectrum approach discussed above, where the smooth spectrum continuum emission is limited to the small delay (or $k_{\parallel}$) modes, but, as opposed to using interferometric visibility spectra, we employ closure phase spectra. The closure phase approach has the distinct advantage of being independent of antenna-based complex gains and hence is robust to calibration terms that are separable into antenna-based contributions (Thomson et al. 2018). For the basics of the closure phase and our power spectral technique, we refer the reader to Thyagarajan et al. (2018) and Carilli et al. (2018). Briefly, the closure phase corresponds to the phase of the triple product, or "bispectrum," of the three complex visibilities measured from three antennas that form a triangle in the array. The closure phase has the important property that the phases introduced by the electronics, and the atmosphere, to each element of the array, cancels in the triple product, such that the closure phase represents a true measure of the attributes of the sky signal, independent of standard antenna-based calibration terms. This interesting property was recognized early in the history of interferometry (Jennison 1958) and has long been used in radio and optical interferometry to infer properties of the sky brightness, in situations where determining antenna-based gains is difficult. For the mathematics, see Thyagarajan et al. (2018) and Carilli et al. (2018).

This is the third in our paper series, in which we present the detailed data and modeling that is then employed in the application of the closure phase technique to Hydrogen Epoch of Reionization Array (HERA) data presented in Thyagarajan et al. (2019), while the initial mathematical foundations for comprehending the bispectrum phase in the context of epoch of reionization (EoR) power spectrum has been detailed in Thyagarajan & Carilli (2020). We employ data from the first season of observations by HERA for a 50 element array. We focus on two fields. First is the field around the transit of the strong radio galaxy, Fornax A. This field provides a number of distinct advantages in testing the closure phase spectral approach to H I 21 cm power spectral estimation. Second is a cold region of the sky with no dominant sources, at J0137-3042.

We present and characterize the data employed and compare them the measured interferometric visibilities, and resulting images, with a detailed modeling of the sky and telescope. Modeling of the sky and telescope is a crucial component of the power spectral analysis, providing the basis of comparison of the measured power spectra to those expected from the foregrounds, the noise, and the H I 21 cm signal (Thyagarajan et al. 2019). The imaging results are a textbook example of strongly confusion-limited imaging in radio interferometry.

For the visibility spectra, we find reasonable broad agreement between data and models over the 80 MHz band, but the models using only point-source models from the GLEAM survey (Hurley-Walker et al. 2017) miss a significant spectral structure on scales of $\sim$10 MHz. We show that this excess spectral structure is likely due to diffuse Galactic emission missing from the GLEAM models. We summarize the potential implications of this missing structure on HERA data analysis and possible mitigation techniques.

2. Hydrogen Epoch of Reionization Array

HERA is an interferometric array designed with the purpose of optimizing the search for the H I 21 cm fluctuations during cosmic reionization using a delay spectrum approach (DeBoer et al. 2017). The array is currently under construction, with a goal of having a 331 element array of 14 m diameter parabolic antennas, distributed in a hexagonal grid pattern, with grid spacing separated by 14.6 m. The antennas are not steerable—the array is a "zenith-only" instrument, at a latitude of $-30^{\circ}.7$.

The primary beam FWHM at 150 MHz is 8.°3, with a maximum baseline for the 331 element array of about 300 m. Another 20 elements will be deployed out to maximum baselines of 1 km.

In this paper, we analyze data from the months of 2018 February to March. We employ the 18 days that comprise HERA Internal Data Release 2.1 (IDR2; Dillon & the HERA Analysis Team 2018). The array at this time consisted of a partial hexagonal array of 50 antennas (HERA-50), with 10.7 s averaging time. The layout of the array used in this analysis can be seen in Figure 2 in Carilli et al. (2018). These data have been inspected for quality assurance. The spectral data have 1024 channels from 100 to 200 MHz, with a channel width of 97 kHz, and full linear polarization.

The data for imaging have been flagged using the standard HERA procedures (Kerrigan et al. 2019). The data have been calibrated using a hybrid process of initial sky-based delay calibration, then redundant baseline calibration, then a sky-based calibration procedure to determine the missing parameters inherent in the redundant baseline calibration process and to determine the absolute gain scale and bandpass (Dillon et al. 2017; Kern et al. 2020).

In the imaging analysis below, we employ the calibrated IDR2 data for imaging as well as amplitude and phase spectral plots. The data have been local sidereal time (LST)-binned over 18 days, meaning each record at a given LST has been averaged over the 18 days to create a single *uv*-data set. We analyze data around the transit of the strong extragalactic radio source, Fornax A (R.A. = 03:22), and around a cold region of the sky at J0137-3042. For the best image presented below of the Fornax field, we also employ a bandpass self-calibration process using a CLEAN component model generated from the data. Self-calibration in the case of Fornax A was required due to the dynamic range issues posed by the large flux density of Fornax A. The standard bandpass calibration process for HERA is weighted toward sources near the pointing center (=zenith), in the calibration fields (Kern et al. 2020). Fornax A, being well down in the primary beam, has a significant residual spectral shape imposed by the primary beam shape as a function of frequency. Hence, prior to self-calibration, the residual sidelobes from Fornax A are large and essentially swamp most of the fainter emission in the field. After bandpass self-calibration using Fornax A itself, these sidelobes are greatly mitigated. Of course, the spectral shape for other sources in the field is not conserved, but that is less relevant for these typically 10–100 times fainter sources, in the final broadband continuum image. However, when analyzing visibility spectra in the amplitude and phase, we plot the original calibrated IDR2 data without bandpass self-calibration. Self-calibration was not employed in the J0137-3042 field.

Imaging is performed with Common Astronomical Software Applications (CASA) CLEAN, using a multifrequency synthesis (MFS; Rau & Cornwell 2011), from 120 to 180 MHz, and Briggs weighting of the visibilities with a robust parameter of −0.5. This weighting results in a synthesized beam of a FWHM = $45' \times 35'$ and a major axis position angle = 65°, at the effective frequency of 150 MHz. We have explored MFS using between 1 and 3 Taylor terms in the imaging and find a small improvement using the higher order. The peak sidelobe of the synthesized beam using the broadband MFS is ∼20%.

In the analysis below, all flux densities, noise values, and related are based on the measured brightnesses in the resulting images.

3. Models versus Data

We selected two fields to explore the visibilities and imaging of the data in comparison to the sky and telescope modeling, in the context of presenting the data that is then used in our closure phase power spectral analysis (Thyagarajan et al. 2019). One field contains a strong, relatively compact source, Fornax A. This field has some interesting characteristics in terms of diagnostics of the closure phase spectra (Carilli et al. 2018). The second is a typical field in a quiet region of the sky.

3.1. The Fornax A Field

Figure 1 is a full-sky radio image at 408 MHz (Haslam et al. 1982). Fornax A is at J0322-3712. Fornax A is situated in one of the coldest regions of the low-frequency sky, with a mean brightness temperature of ∼180 K at 150 MHz (de Oliveira-Costa et al. 2008).

The blue and green lines indicate the horizon for the HERA array for the Fornax field and for the J0137 field discussed below. Notice that large portions of the Galactic plane are always above the horizon for HERA, even for transit observations of the coldest regions of the sky. We return to this point below.

Fornax A is a bright radio source, comprised of two steep spectrum radio lobes, with a full angular extent of the outer boundaries of the radio lobes ∼55′. Hence, Fornax A is marginally resolved in the HERA data presented herein (resolution of ∼40′). Fornax A has a total flux density at 154 MHz of 750 ± 142 Jy and an integrated low-frequency spectral index of about −0.8 (McKinley et al. 2015).

Figure 2 shows the HERA image of the Fornax A field at time of transit, after bandpass self-calibration. We fit a Gaussian model to Fornax A in the HERA image and obtain a total flux density of 173 Jy at the mean frequency of 150 MHz, a peak surface brightness of 120 Jy beam^{-1}, and a nominal deconvolved source FWHM of $36' \times 18'$. The implication is that Fornax A at transit is at the 23% power point of the HERA primary beam. This value is roughly consistent with the primary beam response at the position of Fornax A (6.°5 from the zenith at transit; Fagnoni et al. 2017; Nunhokee et al. 2019). Being well down in the HERA primary beam, Fornax A makes only a minor contribution to the system temperature (∼12 K at 150 MHz at transit, see below). We note that the next brightest source in the HERA beam is ∼8 Jy.

Having a dominant and relatively compact source in the field has a number of distinct advantages when exploring the closure phase spectral approach to detecting the H I 21 cm power spectrum from cosmic reionization. The dominant compact source drives the closure phase to zero, and only small fluctuations, much less than a radian, remain. In Carilli et al. (2018) and Kent et al. (2018), we have shown that the closure phase spectra converge on zero across about ±20 minutes of the transit of Fornax A. Further, in Kent et al. (2018), we show the redundancy of the closure spectra across redundant triads becomes substantially better when Fornax dominates the visibilities. Of course, having a dominant compact source is not a fundamental requirement in the closure phase delay spectrum search for the H I 21 cm signal, as was shown in Thyagarajan et al. (2018), in which more general foreground models were assumed. In Section 3.2, we explore a more general quiet-sky field in both imaging and spectral domain.

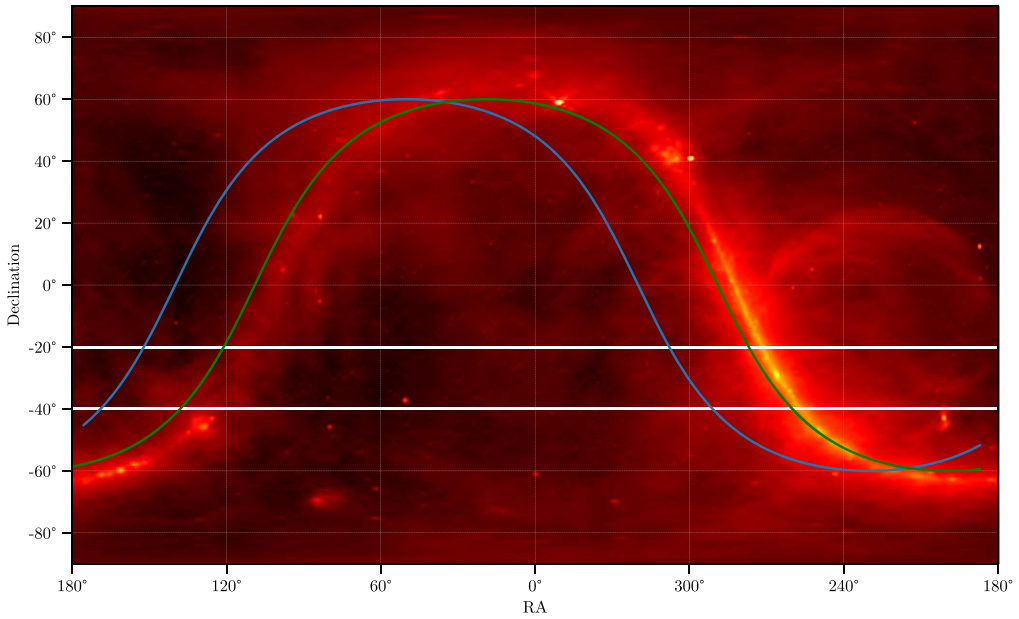

Figure 1. All-sky radio image at 408 MHz from the Haslam survey (Haslam et al. 1982). The solid white lines indicate $\pm 10^{\circ}$ north and south of zenith ($\sim$FWHM of the primary beam at 125 MHz). The blue line shows the horizon at the HERA site, for an LST centered on the Fornax field at transit (Fornax A can be seen at R.A. $= +53^{\circ}$, decl. $= -27^{\circ}$). The green line shows the horizon at transit for the J0137-3042 field.

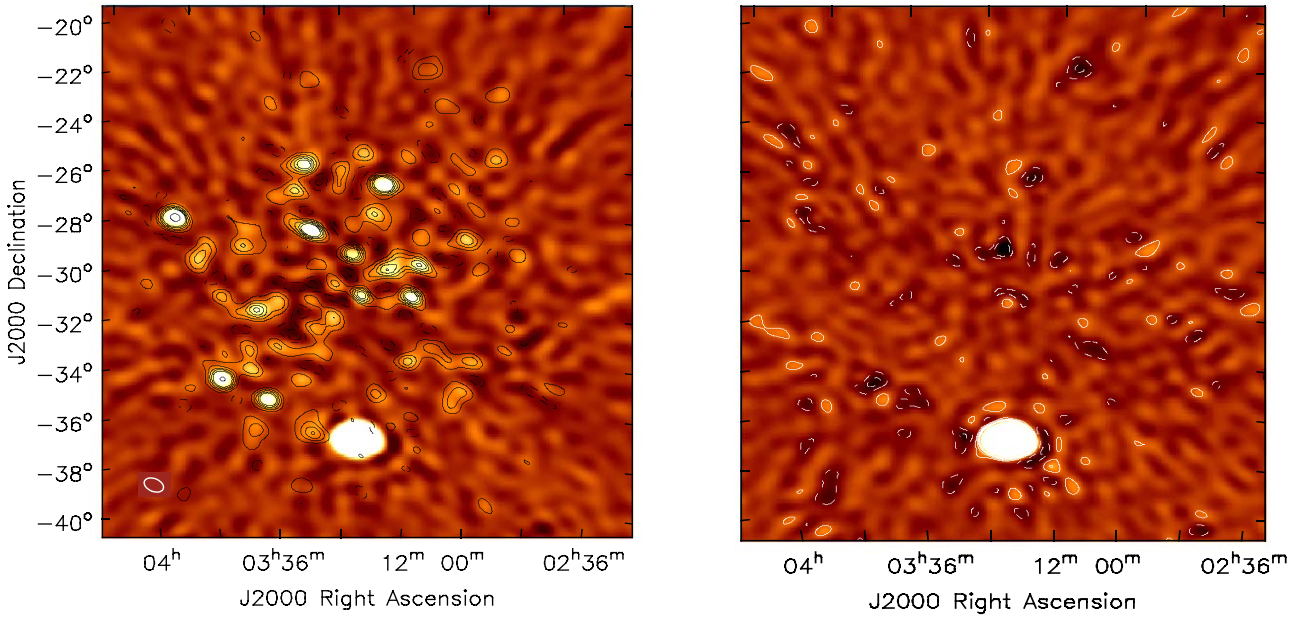

Figure 2. Left: image of the Fornax field using four minutes of data over transit. The color scale shows the image made from the LST-binned IDR2 data from HERA, involving 18 days and using a multifrequency synthesis from 120 to 180 MHz. The contours show the Fornax field GLEAM model, passed through the PRISim simulation and the HERA telescope model to generate visibilities, then imaged in CASA in the exact same way as the real data. The GLEAM model in this case does not include Fornax A itself to better show the underlying distribution of fainter sources. The contour levels are: −1.2, −0.6, 0.6, 1.2, 1.8, 2.4, and 3.0 Jy beam^{-1}, and the resolution is $43' \times 33'$, PA $= 65^{\circ}$. Dashed contours are negative. The rms noise level outside the main beam is 0.4 Jy beam^{-1}. Right: difference image between model and data, with the same contour levels to indicate quantitatively the relative magnitude of the residual features.

We build a model for the Fornax A field, from the GLEAM low-frequency survey (Hurley-Walker et al. 2017). The GLEAM model includes source flux densities at 150 MHz, plus a spectral index determined by the GLEAM survey. We add about 8000 point sources from the GLEAM survey over a 30° diameter area. These correspond to all the sources in the GLEAM catalog over the full region, down to the GLEAM flux density limit of 50 mJy at 154 MHz (5σ). The one exception is Fornax A itself, which is not in the GLEAM catalog and is clearly a very spatially extended radio source. For Fornax A, we used a separate model (Carrollo 2016; P. Carroll & R. Byrne 2020, private communication), based on Murchinson Widefield Array observations from 2013, now in the public archive.

We employ the Precision Radio Interferometry Simulator (PRISim[19]; Thyagarajan et al. 2019) to generate visibilities from the model similar to that in Thyagarajan et al. (2015). We adopt a model for the array using the same antennas that were

[19] PRISim is publicly available for use under the MIT license at https://github.com/nithyanandan/PRISim.

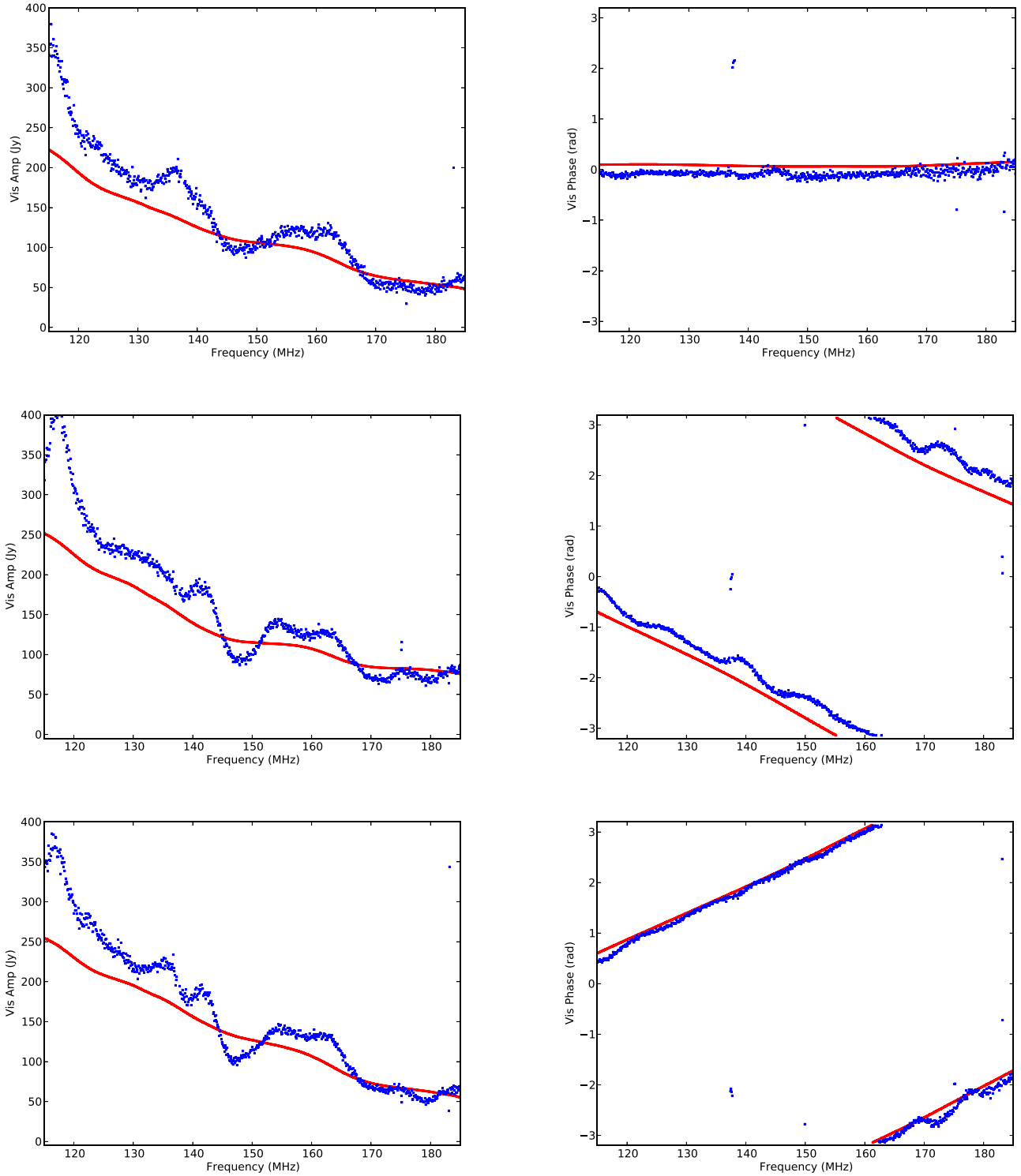

Figure 3. Top (left, right): amplitude and phase spectra on an east–west 29 m baseline for one record at transit of Fornax A. Blue shows the data. Red shows the GLEAM + Fornax A model. Middle: same, but for a 29 m baseline oriented at -30° with respect to north. Bottom: same, but for a 29 m baseline oriented at $+30^{\circ}$ with respect to north.

used during the observations (HERA-50). For the primary beam, PRISim uses the power pattern determined from electromagnetic modeling of the HERA 14 m antenna (Fagnoni et al. 2017). We generate a non-tracking visibility data set for ± 10 minutes around the transit of Fornax A.

We generate visibilities with and without thermal noise. For the purpose of the imaging and visibility model comparisons presented herein, we employ the noiseless data. We show below that the images are confusion limited relative to the expected thermal noise level by more than two orders of magnitude. Including thermal noise makes no discernible difference to the model image results. The thermal noise becomes relevant in the power spectral analysis, as the ultimate limit to detection of the H I 21 cm signal, and we consider thermal noise for HERA in detail in Thyagarajan et al. (2019).

PRISim generates a transit data set in HD5 format. These data are then converted to FITS format and are fringe tracked at the zenith and R.A. of the first record. In the imaging, we employ ±2 minutes around transit of Fornax A. The FITS *uv*-data is converted to a CASA measurement set using pyuvdata tools (Bryna et al. 2017). The same imaging parameters are then employed for the model data as for the observed data.

Figure 2 shows the resulting image of the Fornax A field from the data (color scale) and the GLEAM model (contours). In this case, we did not include Fornax A itself in the simulated model to better show the results for the fainter sources in the field. Figure 2 also shows the difference image, derived by subtracting the model and data images.

Figure 2 shows good agreement between the model image and the observed image. The measured rms of the surface brightness fluctuations outside the primary beam in this image is 0.4 Jy beam^{-1}, while within the primary beam, the rms of the surface brightness fluctuations is about twice this value. Note that these images have not been corrected for the primary beam power response. Hence, the rms noise measured within the primary beam represents confusion noise due to faint sources that fill each synthesized beam (see below). Outside the primary beam, the sky sources are highly attenuated, and the measured noise represents sidelobe confusion noise. For the brighter sources, the flux densities at matched resolutions typically agree to better than 10%. This agreement is comparable to the GLEAM absolute flux density scale uncertainty of 8%, in the relevant decl. range (Hurley-Walker et al. 2017).

The theoretical thermal noise for this HERA-50 image is less than 1 mJy (Parsons & Beardsley 2017; Carilli 2018). The measured rms on the image is 400 times larger. The low resolution of HERA-50 implies that the resulting images are strongly in-beam source confusion limited. Quantitatively, the synthesized beam area is about 0.5 deg^2. The average areal density of GLEAM sources down to 50 mJy is 12 sources per deg^2 at 154 MHz. This implies that there are, on average, six sources brighter than 50 mJy within every synthesized beam of HERA-50, or typically at least 0.3 Jy total flux density per synthesized beam. In other words, thermal noise is not discernible on HERA images. Every synthesized beam is dominated by sources at a level that is orders of magnitude larger than the noise.

Figure 3 shows visibility spectra for one record at Fornax transit, from the IDR2 calibrated data, compared to simulated PRISim visibilities, on the three 29 m baselines that make up an equilateral closure triad in the array. Figure 4 shows the corresponding closure phase spectrum for this triad. The general shape and magnitudes are similar, at the ∼10% level, with the exception that the HERA data spectra show more structure on scales of ∼10 MHz, than the model. We investigate this extra structure below.

3.2. The J0137-3042 Field

The J0137-3042 field is typical of a high Galactic latitude field with no dominant sources. We have modeled this field using the GLEAM catalog, as per the Fornax field modeling above, with about 8000 GLEAM sources included over the 30° × 30° area. The model was then employed, along with a HERA telescope model to generate a visibility data set using both the PRISim software. Images were generated using CASA with parameters as given in Section 2.

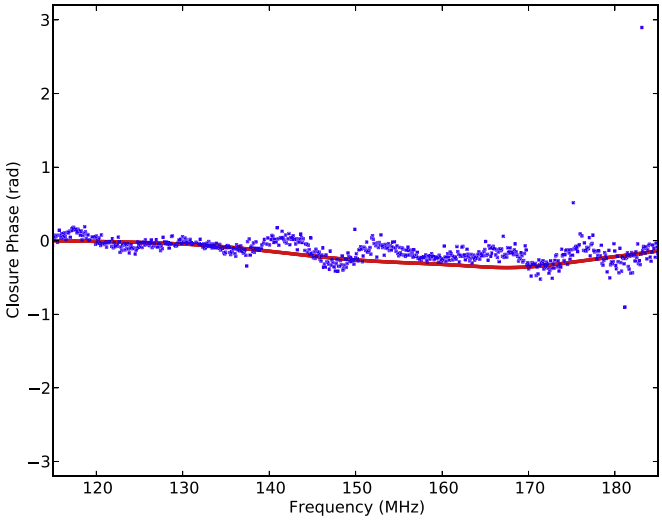

Figure 4. Closure phase spectrum on a 29 m equilateral triad for the Fornax A field at transit. Blue shows the data, and red shows the GLEAM plus Fornax A model.

Figure 5 shows the resulting images for the data itself (color scale) and the model (contours). In this case, no self-calibration was required to reach the confusion noise level. As with the Fornax field, the agreement is very good, down to the confusion level of ∼0.4 Jy beam^{-1}. Figure 5 also shows a difference image between the model and the data. Residuals are predominantly at the noise level, besides at the position of a few of the bright sources, where differences are again ∼10%.

The residual image does show some large-scale structures at the ∼1σ surface brightness level, appearing as rough, broad stripes of positive and negative contours, and extending from the northeast to the southwest, across the primary beam. This large-scale residual may indicate diffuse Galactic emission in the real data that is not included in the GLEAM model. To test this idea, we include in Figure 5, the reprocessed Haslam 408 MHz total power image image of the J0137-3042 field (Haslam et al. 1982; Remazeilles et al. 2016). Evident on the image are large structures oriented along a similar direction, and of similar scale, as the large-scale residuals seen in the HERA difference image. Note that an interferometer has no sensitivity to the total power in the image and indeed to any structures larger than the fringe of the shortest spacing of the array. In our case, this corresponds to scales larger than about 5°. Given such diffuse emission, missing short spacings in an interferometric image will lead to positive and negative artifacts on scales comparable to, or larger than, the shortest fringe spacing of the array, as appears to be the case in the difference image.

Figure 6 shows visibility spectra (amplitude and phase) for three baselines that make up an equilateral 29 m triad, for both the data and the model. Figure 7 shows a similar comparison of the closure spectra for the 29 m equilateral triad. There is good agreement between the large-scale spectral structures between model and data. However, again, the visibility amplitude and phase spectra show considerable smaller-scale structure, in particular. a roughly sinusoidal pattern on frequency scales of ∼10 MHz across the band, with amplitudes of ±20%–50%. This structure is not seen in the model spectra.

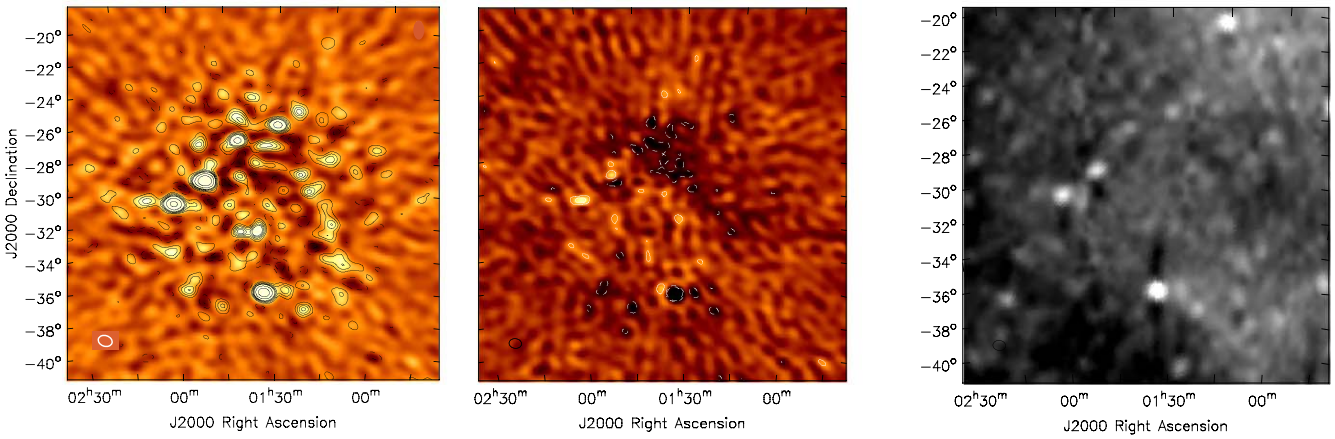

Figure 5. Left: image of the J0137-3042 field using four minutes of data over transit. The color scale shows the image made from the LST-binned IDR2 data from HERA, involving 18 days, using a multifrequency synthesis from 120 to 180 MHz. The contours show the J0137 field GLEAM model, passed through the PRISim simulation and HERA telescope model to generate visibilities, then imaged in CASA in the exact same way as for the real data. The contour levels are: −1.0, −0.5, 0.5, 1.0, 1.5, 2.0, 2.5, 5.0, and 10.0 Jy beam^{-1}, and the resolution is 42′ × 33′, PA = 65°. Dash contours are negative. The rms noise level outside the primary beam is 0.4 Jy beam^{-1}. Middle: difference image between model and data. The contour levels are the same as in the left image to indicate quantitatively the relative magnitude of the residual features. Right: image of the same field, but taken from the all-sky, total power image at 408 MHz of Haslam et al. (1982) and Remazeilles et al. (2016).

4. Modeling Limitations

The resulting images from the GLEAM source models demonstrate clearly the confusion-limited imaging properties of a telescope such as HERA. However, the detail comparison of visibility spectra from GLEAM source-only models with the observed data shows a clear omission of structure in the models, corresponding to an ∼10 MHz scale wavy pattern in the data that is not seen in the model. In this section, we investigate this extra spectral structure and conclude that it is likely due to diffuse Galactic emission filling the far sidelobes of the primary beam and is not captured in a GLEAM-only model. Figure 1, shows that parts of the bright Galactic plane are always above the horizon for HERA, even for the coldest regions of the sky at zenith.

We have generated a model that includes the GLEAM sources for the J0137-3042 field as per Section 3.2 and add a diffuse all-sky model generated from the de Oliveira-Costa et al. (2008) analysis of low-resolution, low-frequency all-sky imaging. We then multiply the models by the full-sky power response of the HERA antenna based on the electromagnetic modeling in Fagnoni et al. (2017). We present two models and the data in Figure 8. One model includes the nominal diffuse sky model at full strength (blue), and the second scales the diffuse model down by a factor of three (red). The factor three down-scaling is arbitrary and simply shows the behavior of the resulting spectra with changes in the strength of the diffuse emission model.

We see that the full strength model overpredicts the observed spectral fluctuations by a large factor, while the fluctuations in the model in which the diffuse emission is down-scaled by a factor of three are closer to those observed. This result demonstrates that, yes the diffuse model addition is likely the cause of the extra spectral structure, but that, unfortunately, our best current knowledge of the far-field beam structure and the diffuse sky does not reproduce the observed visibility structure with any accuracy.

Figure 9 shows the GLEAM sources plus the factor three down-scaled model compared to the measured visibility spectra in the amplitude, phase, and closure phase for a 29 m east–west baseline. The fluctuations in phase and amplitude are of similar magnitude, with similar locations of maxima and minima with frequency, although there remain substantial differences in the details.

Figure 10(a) shows a comparison of the GLEAM plus the scaled diffuse sky model for a 29 and a 44 m east–west baseline. The behavior is as expected, in that the longer baseline has a higher-frequency spectral structure, and is lower amplitude, as the diffuse emission becomes resolved. Extending such an analysis to much longer baselines becomes problematic, since the spectral structure due to the point sources themselves becomes the dominant effect in the measured visibilities.

Figure 10(b) shows a comparison of the model spectra for three 29 m baselines of different orientations. Substantial amplitude differences are seen between the different baseline orientations. Such differences are expected, as the visibility fringe projects along, or transverse, to the large-scale sky structure. Figure 1 shows that, for this particular field, the Galactic plane skirts the entire hemispheric rim, from east to north to west, with the fainter outer galaxy above the horizon to the east and with the brighter inner galaxy just below the horizon to the west, with parts of the thicker disk in the inner galaxy extending above the horizon. Hence, it is not easy to predict which baseline orientation will have the largest amplitude.

Overall, the evidence suggests that the extra spectral structure in visibility spectra not captured in the GLEAM-only model, but seen in the data, is due to diffuse Galactic emission, which is dominated by the bright Galactic plane in the far sidelobes of the primary beam. The challenges of generating a full-sky model including the diffuse Galactic emission plus the extragalactic and Galactic point sources are manifold. First is knowledge of the diffuse emission and its broadband spectral distribution. Second is accurate knowledge of the primary beam as a function of frequency at large zenith angles. Third is the inevitable double counting of the plethora of faint extragalactic and Galactic point sources that appear as a diffuse component at low resolution. This latter effect is particularly problematic in the modeling effort.

Accurate measurement of the far-field primary beam pattern is a severe challenge for non-pointing (zenith) instruments, such as HERA, although techniques using celestial sources are

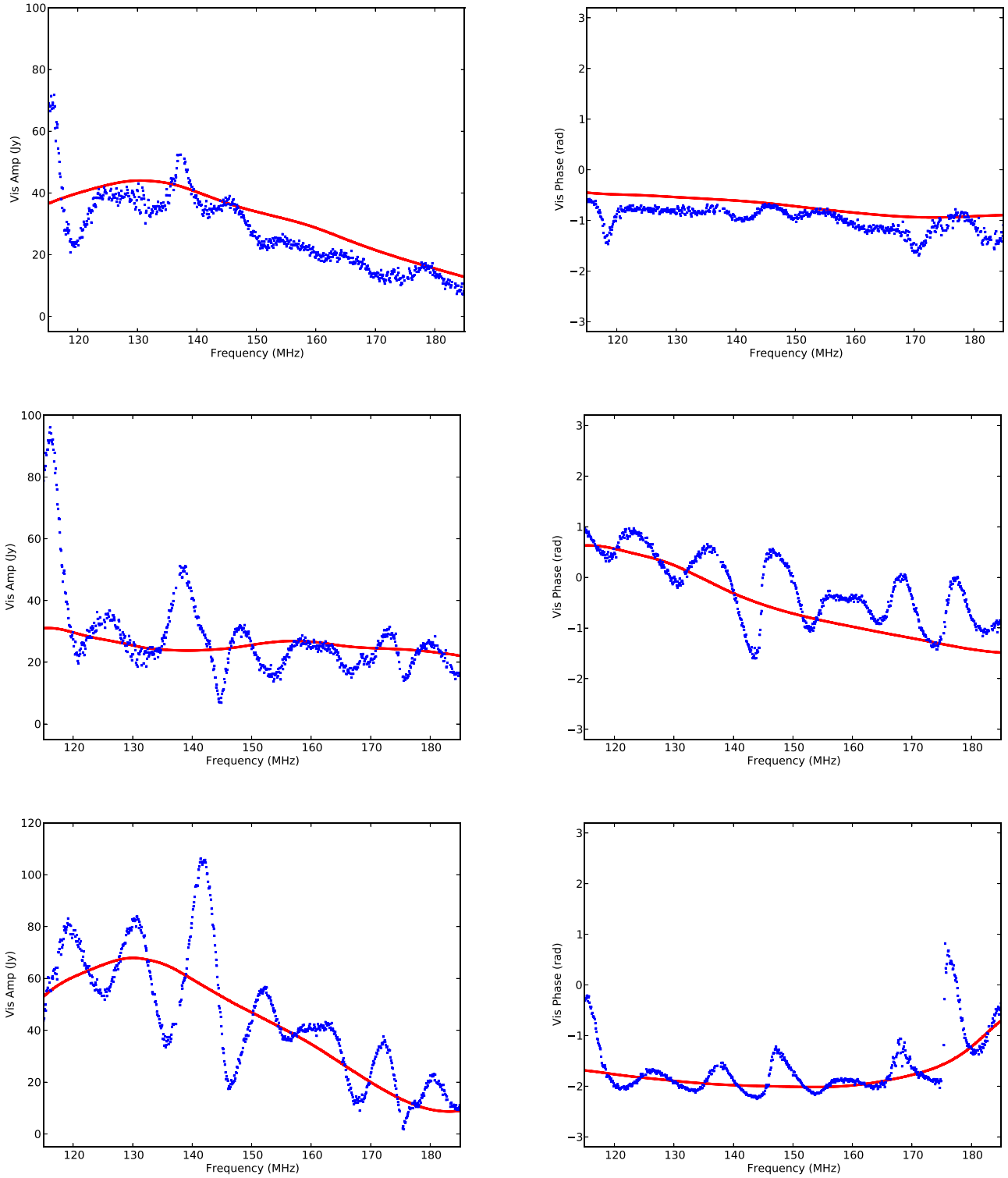

Figure 6. Top (left, right): amplitude and phase spectra on an east–west 29 m baseline for one record at transit of the J0137 field. Red shows a GLEAM point-source–only model. Blue shows the calibrated data. Middle: same, but for a 29 m baseline oriented at -30° with respect to north. Bottom: same, but for a 29 m baseline oriented at $+30^\circ$ with respect to north.

being explored (Pober et al. 2012; Nunhokee et al. 2019). Having an antenna that can point and track over the sky would be clearly advantageous to perform wide-field holography and hence provide a much better measurement of the wide-field primary beam (see Napier 1999). We discuss some of the implications of this spectral structure, and mitigation techniques, below.

5. Discussion

We have made a detailed comparison of HERA-50 visibility spectra and images with sky models generated from the GLEAM survey, plus a HERA telescope model, processed through the PRISim simulator. These models provide an important comparison to the data in our closure phase power

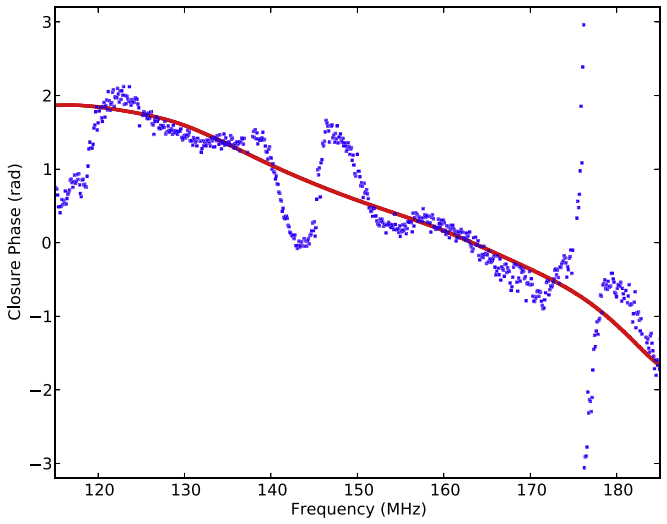

Figure 7. Closure phase spectrum on a 29 m equilateral triad for the J0137 field at transit. Blue shows the data, and red shows the GLEAM point-source model.

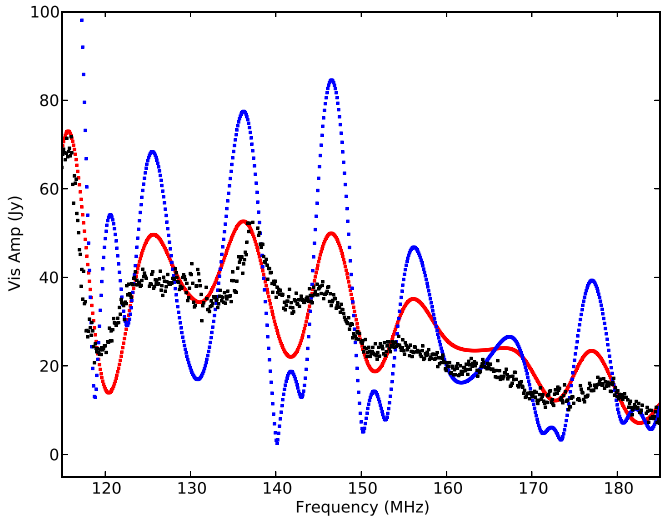

Figure 8. Blue curve shows visibility spectra on a 29 m east–west baseline for a model that includes the GLEAM point sources for the J0137 field, plus a diffuse all-sky model, both weighted by the wide-field telescope primary beam model of Fagnoni et al. (2017, 2019). The red curve shows the same models, but with the diffuse all-sky models scaled down by an arbitrary factor three. The black curve is the observed data.

spectral analysis, in search of the H I 21 cm signal from cosmic reionization (Thyagarajan et al. 2019).

We emphasize that the modeling used in the closure phase power spectral analysis is not required for calibration nor source subtraction, as is required in other power spectral techniques that rely on antenna-based array calibration. The closure phases are independent of simple antenna-based calibration terms, i.e., single antenna-based complex gains per frequency per antenna. Further, the delay spectrum approach limits the smooth spectrum foregrounds to low delay modes and hence is amenable to delay filtering in the power spectrum in order to isolate the H I signal at larger delays (Parsons et al. 2014; Thyagarajan et al. 2019).

For the closure phase power spectral analysis, we require sky models simply to check the scaling of the relative magnitude of effects, such as continuum emission, noise, and the H I 21 cm signal, for comparison to the measured power spectra derived from closure phase spectra. Hence, the required accuracy of the models is very relaxed relative to other techniques. For instance, given the statistical significance of the eventual H I detection with HERA will be at most $\sim$5–10σ for HERA, the modeling accuracy only needs to be good to roughly the 10% level, as a guide for interpreting the closure phase power spectral results (Thyagarajan et al. 2018, 2019).

The results indicate that the images derived from *uv*-data generated using PRISim and a GLEAM survey sky model, plus the HERA-50 telescope model, match the images derived from the real data down to the confusion limit of the telescope of $\sim$0.4 Jy beam^{-1}. The measured noise level in the field is orders of magnitude above the theoretical thermal noise, even for short integrations. HERA-50 is deeply in-beam source confusion limited due to the low spatial resolution and high source areal density at low frequency. An analysis of a residual image between sky and model images, with the total power image of the field, suggests diffuse sky structure at around the confusion level, which is not represented in a point-source–only model.

We conclude that, for the resulting broadband images, the GLEAM sky model, plus the PRISim implementation of the telescope model, is a good representation of the data at the strongly confusion-limited level that can be measured with the HERA array. Correspondingly, the calibrated HERA-50 data generate an image that matches, to the confusion level, what is predicted for the sky surface brightness distribution in these high latitude fields.

For the visibility spectra in the amplitude, phase, and closure phase, there is good agreement of the broad structure across the spectral range, but the measurements themselves show a roughly sinusoidal pattern on scales of $\sim$10 MHz, which is not reproduced in the GLEAM-only model. Adding an all-sky, diffuse emission component, dominated by the Galactic plane at large zenith angles, produces a plausible explanation for this spectral structure. Detailed modeling of this very wide-field sky emission remains problematic due to uncertainties in both the primary beam model and diffuse Galactic emission models, both as a function of frequency, as well as "double counting" of the fainter extragalactic sources that fill the sky.

How will the unmodeled extra spectral structure affect the HERA search for the H I 21 cm signal from cosmic reionization? This question has been considered in Kern et al. (2020) and Thyagarajan et al. (2019), which we briefly summarize.

First is the effect on sky calibration using external models. Any unmodeled structure that is in the data will propagate through the bandpass calibration and lead to errors. This effect has been considered by a number of authors, including Byrne et al. (2019), Li et al. (2019), Barry et al. (2016), van Weeren et al. (2016), and Ewall-Wice et al. (2017). Most recently, Kern et al. (2020) show that the unmodeled spectral structure leads to a peak in the amplitudes in the delay transform at around $\sim$200 nanosec, implying potential contamination of the measured H I 21 cm power spectrum using the delay spectrum approach at low wavenumber $k \sim 0.1\,\mathrm{Mpc}^{-1}$. Fortunately, delay spectrum searches for H I 21 cm emission have thus far relied on analyses at wavenumbers, $k \geqslant 0.2\,\mathrm{Mpc}^{-1}$ (Parsons et al. 2014).

Redundant baseline calibration may be immune to this phenomenon, since it relies on the measured visibilities themselves, but ultimately, remaining degeneracies require that

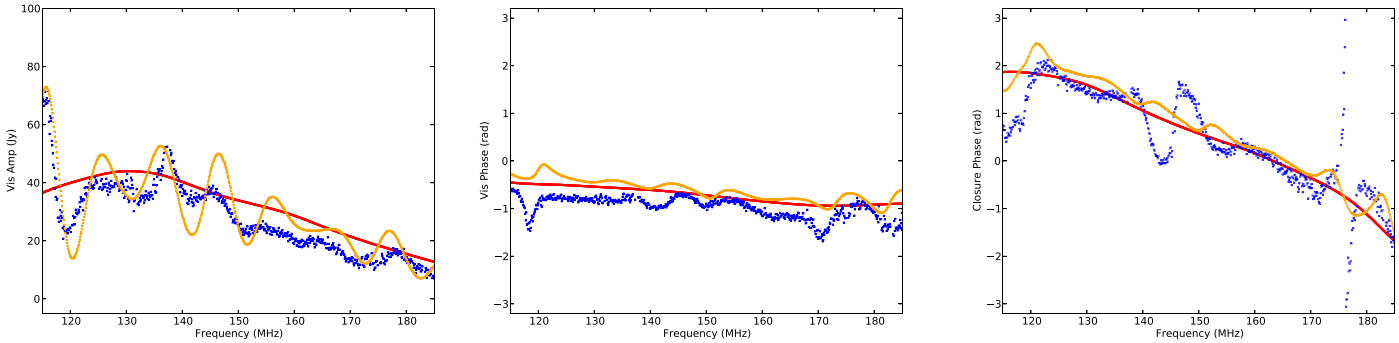

Figure 9. Left: visibility amplitude spectrum for a 29 m east–west baseline in the J0137-3042 field. Blue is the HERA data, and red shows the model including only the GLEAM sources. The orange shows a model including the GLEAM sources, plus a factor three scaled-down all-sky diffuse model, as discussed in Section 4. Center: same, but showing phase. Right: same, but for the closure phase spectrum.

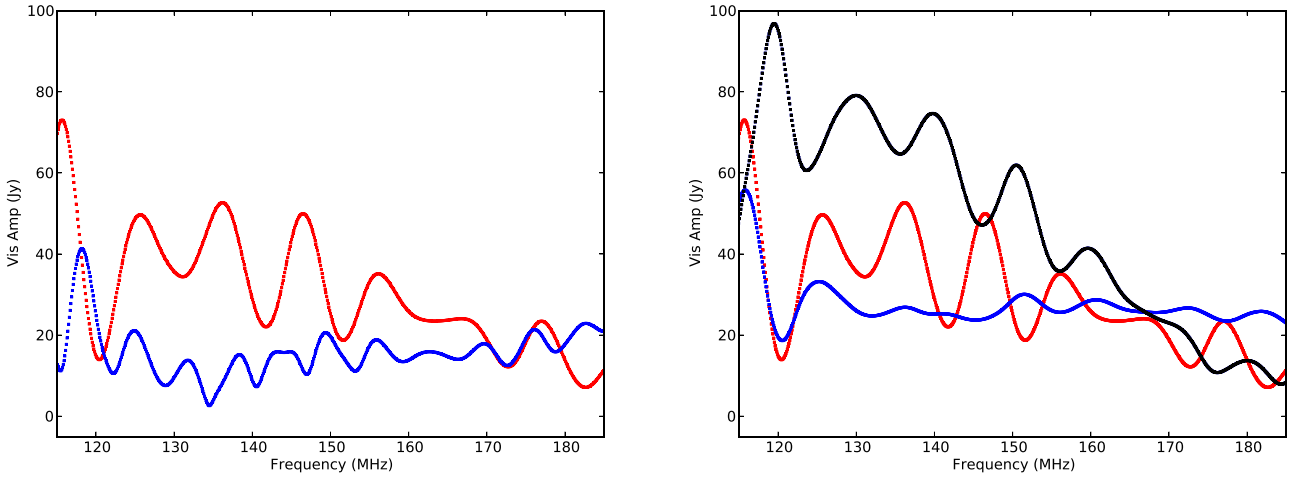

Figure 10. Left: red is the visibility amplitude spectrum for the GLEAM plus the scaled-down diffuse sky model (as show in Figure 8) for a 29 m baseline. Blue is the same, but for a 44 m baseline. Right: red shows the visibility amplitude spectrum for the GLEAM plus the scaled diffuse sky model (as show in Figure 8) for an east–west 29 m baseline. Black shows a 29 m baseline oriented 30° counterclockwise from north. Blue shows a 29 m baseline at 30° clockwise from north.

an average system bandpass be derived based on sky models (Wieringa 1992; Ram Marthi & Chengalur 2014; Dillon & Parsons 2016; Zheng et al. 2017), and hence the problem is not absent (Orosz et al. 2019; Kern et al. 2020).

Self-calibration using models derived from the data itself may perform somewhat better than using a priori sky and telescope models. However, restoring very broad diffuse emission in an interferometric image is a challenge (Rau & Cornwell 2011) and is impossible in cases where the structure is much larger than the shortest spacing of the array. One might consider a process of only using long baselines to calibrate all baselines, since these are less affected by diffuse emission. However, this technique has its own drawbacks, such as higher-frequency residuals across a visibility spectrum due to calibration errors, given the longer baselines involved (Patil et al. 2016; Ewall-Wice et al. 2017).

In terms of the closure phase delay spectrum approach, calibration is not an issue, since the technique employs uncalibrated data. However, any spectral structure on these scales will also show up at similarly low wavenumbers in the power spectrum. If this structure is not paralleled in the modeling, then a comparison of the measured power in the data versus the model at low wavenumbers will not be appropriate (Thyagarajan et al. 2019).

The National Radio Astronomy Observatory is a facility of the National Science Foundation operated under cooperative agreement by Associated Universities, Inc. This material is based upon work supported by the National Science Foundation under grant Nos. 1636646 and 1836019 and institutional support from the HERA collaboration partners. This research is funded in part by the Gordon and Betty Moore Foundation. HERA is hosted by the South African Radio Astronomy Observatory, which is a facility of the National Research Foundation, an agency of the Department of Science and Technology. We gratefully acknowledge the support of NVIDIA Corporation with the donation of the Titan X GPU used for this research. G.B. acknowledges funding from the INAF PRIN-SKA 2017 project 1.05.01.88.04 (FORECaST), support from the Ministero degli Affari Esteri della Cooperazione Internazionale—Direzione Generale per la Promozione del Sistema Paese Progetto di Grande Rilevanza ZA18GR02 and the National Research Foundation of South Africa (grant No. 113121) as part of the ISARP RADIOSKY2020 Joint Research Scheme. C.C., G.B., and S.M. acknowledge support from the Royal Society and the Newton Fund under grant NA150184. This work is based on research supported in part by the National Research Foundation of South Africa (grant No. 103424). N.T. is a Jansky Fellow of the National Radio Astronomy Observatory.

ORCID iDs

C. L. Carilli https://orcid.org/0000-0001-6647-3861
N. Thyagarajan https://orcid.org/0000-0003-1602-7868
N. S. Kern https://orcid.org/0000-0002-8211-1892

G. Bernardi https://orcid.org/0000-0002-0916-7443
James E. Aguirre https://orcid.org/0000-0002-4810-666X
Adam P. Beardsley https://orcid.org/0000-0001-9428-8233
Judd D. Bowman https://orcid.org/0000-0002-8475-2036
Phil Bull https://orcid.org/0000-0001-5668-3101
Joshua S. Dillon https://orcid.org/0000-0003-3336-9958
Aaron Ewall-Wice https://orcid.org/0000-0002-0086-7363
Steve R. Furlanetto https://orcid.org/0000-0002-0658-1243
Bryna J. Hazelton https://orcid.org/0000-0001-7532-645X
Daniel C. Jacobs https://orcid.org/0000-0002-0917-2269
Joshua Kerrigan https://orcid.org/0000-0002-1876-272X
Piyanat Kittiwisit https://orcid.org/0000-0003-0953-313X
Saul A. Kohn https://orcid.org/0000-0001-6744-5328
Matthew Kolopanis https://orcid.org/0000-0002-2950-2974
Adrian Liu https://orcid.org/0000-0001-6876-0928
Miguel F. Morales https://orcid.org/0000-0001-7694-4030
Abraham R. Neben https://orcid.org/0000-0001-7776-7240
Nipanjana Patra https://orcid.org/0000-0002-9457-1941
Jonathan C. Pober https://orcid.org/0000-0002-3492-0433
Peter K. G. Williams https://orcid.org/0000-0003-3734-3587

References

Barry, N., Hazelton, B., Sullivan, I., Morales, M. F., & Pober, J. C. 2016, MNRAS, 461, 3135
Barry, N., Wilensky, M., Trott, C. M., et al. 2019, ApJ, 884, 1
Beardsley, A. P., Hazelton, B. J., Sullivan, I. S., et al. 2016, ApJ, 833, 102
Bryna, J. H., Daniel, C. J., Jonathan, C. P., & Adam, P. B. 2017, JOSS, 2, 140
Byrne, R, Morales, M. F., Hazelton, B., Li, W., & Barry, N. 2019, ApJ, 875, 70
Carilli, C. L. 2018, HERA Memo Ser. 060, http://reionization.org/science/memos/
Carilli, C. L., Nikolic, B., Thyagarayan, N., et al. 2018, RaSc, 53, 845
Carrollo, P. A. 2016, PhD thesis, Univ. Washington
Chapman, E., Abdalla, F., Bobin, J., et al. 2013, MNRAS, 429, 165
Datta, A., Carilli, C. L., & Bowman, J. 2010, ApJ, 724, 526
de Oliveira-Costa, A., Tegmark, M., Gaensler, B. M., et al. 2008, MNRAS, 388, 247
DeBoer, D. R., Parsons, A. R., Aguirre, J. E., et al. 2017, PASP, 129, 5001
Dillon, J., Liu, A., Kohn, S., Kern, N., & Parsons, A. 2017, HERA Memo Ser. 030, http://reionization.org/science/memos/
Dillon, J., & Parsons, A. 2016, ApJ, 826, 181
Dillon, J. & the HERA Analysis Team 2018, HERA Memo Ser. 045, http://reionization.org/science/memos/
Ewall-Wice, A., Dillon, J. S., Liu, A., & Hewitt, J. 2017, MNRAS, 470, 1849
Fagnoni, N., de Lera Acedo, E., DeBoer, D. R., et al. 2019, MNRAS, submitted (arXiv:1908.02383)
Fagnoni, N., De Lera Acedo, E., & Kolitsidas, C. 2017, HERA Memo Ser. 029, http://reionization.org/science/memos/
Fan, X., Carilli, C. L., & Keating, B. 2006, ARA&A, 44, 415
Furlanetto, S. R., Peng Oh, S., & Briggs, F. H. 2006, PhR, 433, 181
Greig, B., & Mesinger, A. 2015, MNRAS, 449, 4246
Greig, B., & Mesinger, A. 2017, MNRAS, 465, 4838
Harker, G., Zaroubi, S., Bernardi, G., et al. 2009, MNRAS, 397, 1138
Harker, G., Zaroubi, S., Bernardi, G., et al. 2010, MNRAS, 405, 2492
Haslam, C. G. T., Salter, C. J., Stoffel, H., & Wilson, W. E. 1982, A&AS, 47, 1
Hurley-Walker, N., Callingham, J. R., Hancock, P. J., Franzen, T. M. O., & Hindson, L. 2017, MNRAS, 464, 1146
Jennison, R. C. 1958, MNRAS, 118, 276
Kent, J., Nikolic, B., Carilli, C., et al. 2018, HERA Memo Ser. 055, http://reionization.org/science/memos/
Kern, N. S., Dillon, J. S., Parsons, A. R., et al. 2020, ApJ, 890, 122
Kerrigan, J., La Plante, P., Kohn, S., et al. 2019, MNRAS, 488, 2605
Kolopanis, M., Jacobs, D. C., Cheng, C., et al. 2019, ApJ, 883, 133
Li, W., Pober, J. C., Barry, N., et al. 2019, ApJ, 887, 141
Loeb, A., & Furlanetto, S. 2013, The First Galaxies in the Universe (Princeton, NJ: Princeton Univ. Press)
McKinley, B., Yang, R., López-Caniego, M., et al. 2015, MNRAS, 446, 3478
Morales, M. F. 2005, ApJ, 619, 678
Morales, M. F., Beardsley, A., Pober, J., et al. 2019, MNRAS, 483, 2207
Morales, M. F., & Wythie, J. S. 2010, ARA&A, 48, 127
Napier, P. 1999, in ASP Conf. Ser. 180, Synthesis Imaging in Radio Astronomy, ed. C. P. Taylor (San Francisco, CA: ASP), 37
Noordam, J. E. 2004, Proc. SPIE, 5489, 817
Nunhokee, C. D., & Parsons, A. R. 2019, HERA Memo Ser. 065, http://reionization.org/science/memos/
Orosz, N., Dillon, J. S., Ewall-Wice, A., Parsons, A. R., & Thyagarajan, N. 2019, MNRAS, 487, 537
Parsons, A., & Beardsley, A. 2017, HERA Memo Ser. 034, http://reionization.org/science/memos/
Parsons, A. R., Liu, A., Aguirre, J. E., et al. 2014, ApJ, 788, 106
Patil, A. H., Yatawatta, S., Koopmans, L. V. E., et al. 2017, ApJ, 838, 65
Patil, A. H., Yatawatta, S., Zaroubi, S., et al. 2016, MNRAS, 463, 4317
Pober, J. C., Parsons, A. R., Jacobs, D. C., et al. 2012, AJ, 143, 53
Ram Marthi, V., & Chengalur, J. 2014, MNRAS, 437, 524
Rau, U., & Cornwell, T. J. 2011, A&A, 532, 71
Remazeilles, M., Dickinson, C., Eriksen, H. K. K., & Wehus, I. K. 2016, MNRAS, 458, 2032
Tegmark, M. 1997, PhRvD, 55, 5895
Thomson, R. A., Moran, J., & Swenson, G. W. 2018, Interferometry and Synthesis in Radio Astronomy (Berlin: Springer)
Thyagarajan, N., & Carilli, C. L. 2020, PhRvD, submitted (Paper IV)
Thyagarajan, N., Carilli, C. L., & Nikolic, B. 2018, PhRvL, 120, 251301
Thyagarajan, N., Carilli, C. L., Nikolic, B., et al. 2019, PhRvD, submitted (Paper V)
Thyagarajan, N., Daniel, C. J., Judd, D. B., et al. 2015, ApJ, 804, 14
Thyagarajan, N., Kolopanis, M., Jacobs, D., & Murray, S. 2019, nithyanandan/PRISim v0.2-alpha, Zenodo, doi:10.5281/zenodo.2548117
Trott, C. M., Jordan, C. H., Midgley, S., et al. 2020, MNRAS, 493, 4711
van Weeren, R. J., Williams, W. L., Hardcastle, M. J., et al. 2016, ApJS, 223, 2
Wieringa, M. H. 1992, ExA, 2, 203
Zaldarriaga, M., Furlanetto, S. R., & Hernquist, L. 2004, ApJ, 608, 622
Zaroubi, S. 2013, ASSL, 396, 45
Zheng, H., Tegmark, M., Dillon, J. S., et al. 2017, MNRAS, 465, 2901